

This discussion paper is/has been under review for the journal Atmospheric Measurement Techniques (AMT). Please refer to the corresponding final paper in AMT if available.

A novel method for estimating shortwave direct radiative effect of above-cloud aerosols using CALIOP and MODIS data

Z. Zhang^{1,2}, K. Meyer^{3,4}, S. Platnick⁴, L. Oreopoulos⁴, D. Lee^{4,5}, and H. Yu^{4,6}

¹Department of Physics, University of Maryland, Baltimore County (UMBC), Baltimore, MD, USA

²Joint Center Earth Systems & Technology (JCET), UMBC, Baltimore, MD, USA

³Goddard Earth Sciences Technology and Research (GESTAR), Universities Space Research Association, Columbia, MD, USA

⁴NASA Goddard Space Flight Center, Greenbelt, Maryland, USA

⁵Goddard Earth Sciences Technology and Research (GESTAR), Morgan State University, Baltimore, MD, USA

⁶Earth System Science Interdisciplinary Center, University of Maryland, College Park, MD, USA

Received: 28 October 2013 – Accepted: 8 November 2013 – Published: 15 November 2013

Correspondence to: Z. Zhang (zhibo.zhang@umbc.edu)

Published by Copernicus Publications on behalf of the European Geosciences Union.

9993

Abstract

This paper describes an efficient and unique method for computing the shortwave direct radiative effect (DRE) of aerosol residing above low-level liquid-phase clouds using CALIOP and MODIS data. It accounts for the overlapping of aerosol and cloud rigorously by utilizing the joint histogram of cloud optical depth and cloud top pressure. Effects of sub-grid scale cloud and aerosol variations on DRE are accounted for. It is computationally efficient through using grid-level cloud and aerosol statistics, instead of pixel-level products, and a pre-computed look-up table in radiative transfer calculations. We verified that for smoke over the southeast Atlantic Ocean the method yields a seasonal mean instantaneous shortwave DRE that generally agrees with more rigorous pixel-level computation within 4 %. We have also computed the annual mean instantaneous shortwave DRE of light-absorbing aerosols (i.e., smoke and polluted dust) over global ocean based on 4 yr of CALIOP and MODIS data. We found that the variability of the annual mean shortwave DRE of above-cloud light-absorbing aerosol is mainly driven by the optical depth of the underlying clouds.

1 Introduction

The shortwave direct radiative effect (DRE) of aerosols at the top of the atmosphere (TOA) is strongly dependent on the reflectance of the underlying surface. Over dark surfaces (e.g. ocean, vegetated land), the scattering effect of aerosols is generally dominant, leading to negative DRE (i.e., cooling) at TOA (Yu et al., 2006). In contrast, when light-absorbing aerosols occur above clouds or other bright surfaces (such as snow, ice, desert), aerosol absorption is significantly amplified by cloud or surface reflection, offsetting or even exceeding the scattering effect of the aerosol leading to a less negative or even positive (i.e., warming) TOA DRE (Abel et al., 2005; Keil and Haywood, 2003; Twomey, 1977). Therefore, in order to understand the full complexity of aerosol radiative effects on climate, it is important to quantify the DRE under

9994

both clear-sky and cloudy-sky conditions. Although the DRE of aerosols in clear-sky regions has been extensively studied and is relatively well constrained based on advanced satellite remote sensing measurements acquired in the last decade (Yu et al., 2006), the cloudy-sky DRE is generally assumed to be negligible or simulated by models (Schulz et al., 2006). Current model simulations show a large inter-model spread in cloudy-sky DRE (Schulz et al., 2006), which results from inter-model differences in both aerosol and cloud properties (Schulz et al., 2006; Stier et al., 2013). There is a clear need for an observational constraint on the DRE of above-cloud aerosol (ACA).

Recent advances in satellite remote sensing techniques have provided an unprecedented opportunity for studying the DRE of ACA. In particular, the availability of measurements from the space-borne Cloud-Aerosol Lidar with Orthogonal Polarization (CALIOP) sensor onboard NASA's Cloud-Aerosol Lidar and Infrared Pathfinder Satellite Observations (CALIPSO) satellite has provided a revolutionary global view of the vertical distribution of aerosols and clouds (e.g., Winker et al., 2013). Using CALIOP aerosol and cloud layer products, Devasthale and Thomas (2011) found frequent occurrences of aerosols residing above low-level clouds in several regions of the globe. In particular, they found a high frequency of smoke occurrence over low clouds in the southeast Atlantic, western coasts of South America (e.g., Columbia, Ecuador, and Peru) and southern Asia. These authors also found a high frequency of natural and polluted dust aerosols overlapping low clouds off the western coasts of Saharan Africa in boreal summer and over the eastern coast of China in boreal spring (see Fig. 3 of Devasthale and Thomas, 2011).

CALIOP measurements of ACA properties, in combination with satellite cloud products from, for example, the Moderate Resolution Imaging Spectroradiometer (MODIS), have been used in several recent studies to derive the DRE of ACA with radiative transfer simulations (e.g., Chand et al., 2009; Costantino and Bréon, 2013b; Oikawa et al., 2013). Chand et al. (2009) used CALIOP above-cloud AOD retrievals (Chand et al., 2008) and Terra-MODIS cloud products, both aggregated to 5° gridded monthly means, to calculate the radiative effects of smoke transported above the low-level

9995

stratocumulus deck in the southeastern Atlantic. A major point made in this study is that the all-sky DRE of elevated light-absorbing aerosols, such as transported smoke, is strongly modulated by the underlying cloud properties. However, the spatial-temporal aggregation of both CALIOP and MODIS data to coarse gridded monthly means obscures the potential influence of cloud and aerosol variability on the DRE. In particular, using grid box mean cloud optical depth for DRE calculation might lead to biases in DRE due to the plane-parallel albedo bias (Oreopoulos et al., 2007; Min and Zhang, 2013). Moreover, the MODIS level-3 aggregation algorithm samples all liquid water clouds, regardless of possible retrieval contamination by ACA. As a result, the total population of liquid water clouds in the MODIS level-3 products (daily or monthly) may be significantly different from that of below-aerosol-only cloud population. Therefore, using level-3 MODIS products without distinguishing below-aerosol-only cloud population from the total can potentially lead to significant errors. The problem could be further complicated by biases in MODIS cloud retrievals associated with the presence of overlying light-absorbing aerosols. When a cloud-pixel is contaminated by overlying light-absorbing aerosols the MODIS cloud optical depth (COD) retrieval is generally biased low (Coddington et al., 2010; Haywood et al., 2004), an effect not considered in most previous studies (e.g., Chand et al., 2009; Costantino and Bréon, 2013b; Oikawa et al., 2013). Meyer et al. (2013) found that correcting the MODIS COD bias due to ACA contamination can lead to a more positive ACA DRE.

Most recently, Meyer et al. (2013) collocated CALIOP above-cloud AOD and Aqua-MODIS cloud properties at pixel level, and the DRE was then computed at individual collocated pixels. Such rigorous collocation has obvious advantages as it takes into account the sub-grid variability of clouds and aerosols. However, such a method is computationally expensive and requires large amounts of pixel-level data, which poses a major challenge for application on a global scale and multiyear basis.

The objective of this paper is to describe a novel method for computing the DRE of ACA. In this method, we attempt to balance the need for computational efficiency with the need for rigorous treatment of aerosol-cloud overlapping and small-scale

9996

variabilities of aerosol and clouds. Our method has several unique features: (1) it takes sub-grid scale cloud and aerosol variation into account in DRE computation; (2) it treats the overlapping of aerosol and cloud rigorously by utilizing the joint histogram of cloud optical depth and cloud top pressure in the MODIS level-3 product; (3) it is computationally efficient because of the use of a pre-computed look-up table of ACA DRE. In the following sections, we briefly introduce the CALIOP and MODIS data used (Sect. 2), describe the key assumption and features of the method (Sect. 3), validate it through comparison with pixel-level computations as in Meyer et al. (2013) (Sect. 4), and conclude with a summary and discussion (Sect. 5).

10 2 Satellite data

2.1 CALIOP aerosol and cloud layer products

Since its launch in 2006, the space-borne lidar CALIOP has continuously acquired, with near global (albeit instantaneously sparse) coverage, attenuated backscatter measurements at 532 nm and 1064 nm, including linear depolarization information at 532 nm (Winker et al., 2009). The CALIOP level-2 retrieval algorithm consists of several steps. First, a “feature finder” algorithm and cloud-aerosol discrimination (CAD) algorithm are used to detect aerosol and cloud layers, and record their top and bottom heights and layer integrated properties (Vaughan et al., 2009). Second, the detected aerosol layers are further classified into six sub-types (i.e., polluted continental, biomass burning, desert dust, polluted dust, clean continental and marine) (Omar et al., 2009) and cloud layers into different thermodynamic phases (Hu et al., 2007) based on the observed backscatter, color ratio and depolarization ratio. Third, a priori lidar ratios, selected based on aerosol sub-type and cloud phase, are used to derive the extinction of an aerosol or cloud layer from the attenuated backscatter profile (Young and Vaughan, 2008).

9997

In this study, we use CALIOP level-2 version 3 aerosol and cloud layer products at a nominal 5 km horizontal resolution (i.e., CAL_LID_L2_05kmALay and CAL_LID_L2_05kmCLay) for aerosol-cloud overlapping detection, and for information on aerosol layer properties, including aerosol layer type, aerosol optical depth (AOD), and layer top and bottom height. In addition to physical properties, the CALIOP layer products also provide various metrics and flags for data quality assurance. These include CAD score (Liu et al., 2009), horizontal averaging scale, the extinction quality control (QC) flag, and estimated uncertainty for layer AOD. In this study, we use these metrics following the best practice advice of the CALIPSO science team to screen for reliable retrievals (e.g., Winker et al., 2013) (see Table 1).

2.2 MODIS daily level-3 cloud property product

We use the Collection 5 (C5) Aqua MODIS level-3 daily gridded Atmosphere product (i.e., MYD08_D3) for cloud properties and other parameters, such as solar zenith angle, needed for ACA DRE computations. The MODIS level-3 gridded products are aggregated at 1° resolution from the MODIS level-2 pixel-level retrievals (Hubanks et al., 2008; King et al., 2003). As summarized in Platnick et al. (2003), the operational level-2 MODIS cloud product provides cloud masking (Ackerman et al., 1998), cloud top height retrieval based on CO_2 slicing or the infrared window method (Menzel et al., 1983), cloud top thermodynamic phase determination (Menzel et al., 2006), and cloud optical and microphysical property retrieval based on the bi-spectral solar reflectance method (Nakajima and King, 1990). In addition to these cloud parameters, the level-2 products also provide pixel-level runtime Quality Assessment (QA) information, which includes product quality as well as processing path information.

All MODIS level-2 atmosphere products, including the cloud, aerosol and water vapor products, are aggregated to 1° spatial resolution on a daily, eight-day, and monthly basis. Aggregations include a variety of scalar statistical information (mean, standard deviation, max/min occurrences) and histograms (marginal and joint). A particularly useful level-3 cloud product for this study is the daily joint histogram of cloud optical

9998

depth (COD) vs. cloud top pressure (CTP), derived using daily counts of successful level-2 pixel retrievals that fall into each joint COD-CTP bin. Eleven COD bins, ranging from 0 to 100, and 13 CTP bins, ranging from 200 to 1000 mb, comprise the histogram. As discussed below, the COD-CTP joint histogram allows for identifying the portion of the cloud population that lies beneath the aerosol layer found by CALIOP, as well as the corresponding COD probability distribution needed for DRE estimation. In addition to the COD-CTP joint histogram, we also use the gridded mean solar and sensor zenith angles for calculating DRE and correcting COD bias associated with ACA.

3 Methodology

10 3.1 Theoretical basis

As in previous investigations (e.g., Chand et al., 2008, 2009; Costantino and Bréon, 2013b; Meyer et al., 2013), we focus on the simplest case of overlapping aerosol and cloud, i.e., a single layer of aerosol overlying a single layer of low-level liquid-phase clouds, which is commonly observed in many regions of the globe (Devasthale and Thomas, 2011). More complex situations exist, such as an aerosol layer located in between high cloud and low cloud, or an aerosol layer overlying multiple layers of clouds. However, such situations are either beyond the capability of CALIOP or relatively rare (Devasthale and Thomas, 2011). As such, they are left for future research and are not considered here.

20 To illustrate the theoretical foundation of the method, consider the schematic example in Fig. 1. For a given grid box, the gridded mean broadband shortwave DRE ($\langle \text{DRE} \rangle_{\text{ACA}}$) averaged over all ACA pixels within the grid box is given by:

$$\langle \text{DRE} \rangle_{\text{ACA}} = \int_0^{\infty} \int_0^{\infty} \text{DRE}(\tau_c, \tau_a) p(\tau_c, \tau_a) d\tau_c d\tau_a, \quad (1)$$

9999

where $p(\tau_c, \tau_a)$ is the joint probability density function (PDF) of the above-cloud AOD at 532 nm (τ_a) and below-aerosol COD (τ_c) of ACA pixels. We note that, in addition to τ_a , DRE is also a function of wavelength dependence of AOD, spectral single scattering albedo and asymmetry factor, which are not explicitly included in this equation. These properties are computed using a Mie scattering code (Wiscombe, 1980) based on the aerosol model described in Meyer et al. (2013). The dependencies on solar zenith angle, surface reflectance, cloud particle effective radius, and atmospheric profile are also omitted; solar zenith angle and surface reflectance are expected to have only minor variation within the grid box, while the impact of cloud particle effective radius and atmospheric profile on shortwave DRE is relatively small. Since $p(\tau_c, \tau_a)$ describes the covariation of aerosols and clouds for the ACA pixels, it should ideally be derived from collocated CALIOP aerosol and MODIS cloud retrievals at pixel level as in Meyer et al. (2013). This requires large amounts of pixel-level data, however, as one month of global daytime C5 MODIS level-2 cloud products in HDF format are roughly 150 Gb. Therefore, pixel-level collocation and radiative transfer simulation are too computationally expensive and cumbersome for multiyear global studies.

A key assumption in our method, which allows us to avoid tedious pixel-level collocation, is that above-cloud AOD and below-aerosol COD are statistically independent. Under this assumption, $p(\tau_c, \tau_a) = p(\tau_c) \cdot p(\tau_a)$ and Eq. (1) reduces to:

$$20 \quad \langle \text{DRE} \rangle_{\text{ACA}} = \int_0^{\infty} \left[\int_0^{\infty} \text{DRE}(\tau_c, \tau_a) p(\tau_c) d\tau_c \right] p(\tau_a) d\tau_a, \quad (2)$$

where $p(\tau_c)$ and $p(\tau_a)$ are the PDF of below-aerosol COD τ_c and above-cloud AOD τ_a , respectively, of ACA pixels. The advantage of Eq. (2) is that it allows $p(\tau_c)$ and $p(\tau_a)$ to be derived separately and independently. This assumption is reasonable considering that transported ACAs and low-level boundary layer clouds are usually well separated vertically (Devasthale and Thomas, 2011) and controlled by different meteorological conditions. The potential coupling between the two is that overlying absorbing

10000

aerosols could influence the evolution of clouds through changing atmospheric stratification (Wilcox, 2010). However, a recent observational study (Costantino and Bréon, 2013a) found no correlation between above-cloud AOD and below-aerosol COD. Moreover, as shown in Sect. 4, we have compared the DRE derived from pixel-level collocation (i.e., based on Eq. 1) with that from independent sampling of $p(\tau_c)$ and $p(\tau_a)$ (i.e., based on Eq. 2) and found very good agreement.

In our method, the PDF of above-cloud AOD $p(\tau_a)$ is derived from the CALIOP 5 km aerosol and cloud layer products through the following steps: (1) for each 5 km CALIOP profile that falls within a given latitude-longitude grid box, we first search for an aerosol layer; (2) if an aerosol layer is detected and the quality metrics pass the quality assurance criteria summarized in Table 1, we then proceed to check for the presence of an underlying liquid-phase cloud layer within the profile using the CALIOP cloud layer product; (3) if a cloud layer is present, the AOD of the aerosol layer is recorded for the derivation of the $p(\tau_a)$ of the grid box. The bottom height of the aerosol layer is also recorded to derive the grid mean aerosol layer bottom height. Once all of the CALIOP profiles within the grid box are processed, we obtain the PDF of the above-cloud AOD $p(\tau_a)$ and the mean aerosol layer bottom pressure $\langle P_{\text{bottom}} \rangle$.

As schematically illustrated in Fig. 1, the PDF of below-aerosol COD $p(\tau_c)$ is derived from the joint histogram of cloud optical depth and cloud top pressure (COD-CTP joint histogram) in the MODIS daily level-3 product, using the grid mean aerosol layer bottom pressure $\langle P_{\text{bottom}} \rangle$ derived above. For a given grid box, we first identify the population of liquid-phase clouds below the pressure level $\langle P_{\text{bottom}} \rangle$. This subset, together with the AOD PDF $p(\tau_a)$, is then used to calculate DRE according to Eq. (2).

3.2 DRE look-up tables

For better computational efficiency, we use pre-computed aerosol-type specified look-up-tables (LUTs), instead of online radiative transfer computation, when deriving the DRE of ACA. The concept of our LUTs is somewhat similar to the “radiative kernels” described in Hartmann et al. (2001) and Zelinka et al. (2012) for computing cloud

10001

radiative feedbacks. The LUT for each aerosol type consists of DREs at both TOA and surface (not used in this study) for various combinations of AOD, COD, CTP and solar zenith conditions. As such, once the aerosol type and AOD are known from CALIOP and COD, CTP and solar zenith angle are known from MODIS, the corresponding DRE can be obtained through LUT interpolation. Note that the CALIOP only provides AOD at lidar wavelengths (e.g., 532 nm and 1064 nm) for each aerosol type. Therefore, broadband aerosol scattering properties, including spectrally dependent AOD, single-scattering albedo and asymmetry factor, are needed for the development of LUT. The current version of LUT focuses on light-absorbing aerosols (e.g., smoke and polluted dust). In order to validate our method with more rigorous pixel-level computations, we adopt the broadband aerosol optical properties from Meyer et al. (2013) in the computation of the current LUT. The aerosol model in Meyer et al. (2013) is extended from an absorbing aerosol model developed for the MODIS Collection 5 Aerosol Product (MOD04) (see Table 4 of Levy et al., 2009). The MOD04 aerosol models define aerosol size distributions and refractive indices dependent solely on prescribed AOD at 550 nm (MODIS band 4; note that the absorbing aerosol model used here assumes a constant index of refraction, $1.51 - 0.02i$, at all wavelengths). At AOD = 0.5 at 550 nm, the single-scattering albedo of this model is about 0.9 over the visible spectral region (see Fig. 7 of Meyer et al., 2013), which is in the range of previously reported values (e.g., Keil and Haywood, 2003; Myhre et al., 2003). The current AOD bins (at 550 nm) in the LUT range from 0.05 to 1.5, which covers most of the above-cloud AOD observed by CALIOP. The current COD bins, logarithmically spaced, range from 0.1 to 300. Following the MODIS level-3 data, the thirteen CTP bins range from 1000 mb to 200 mb. The solar zenith angle bins range from 0 to 80°. Radiative transfer computations are carried out using the RRTM-SW model (Clough et al., 2005; Iacono et al., 2008). Lambertian ocean surface reflectance is set to 5 %. Cloud droplet effective radius is fixed at 15 µm, which is close to the global mean value over oceans observed by MODIS (King et al., 2013). Water cloud optical properties are calculated internally by RRTM. For atmospheric profiles of water vapor and temperature, we use NCEP R1 reanalysis

10002

data (Kistler et al., 2001) averaged both zonally and annually. Our sensitivity tests indicate that the shortwave DRE of ACA is very insensitive to cloud effective radius or atmospheric profiles.

3.3 Cloud optical depth correction

5 As noted in previous studies (Coddington et al., 2010; e.g., Haywood et al., 2004), when
a cloudy MODIS pixel is contaminated by overlying light-absorbing aerosols the COD
retrieval is generally biased low. We have developed a fast COD correction scheme to
account for the COD retrieval bias due to ACA in our DRE computation, which is illus-
trated in Fig. 2. This scheme requires both the cloud reflectance LUT for clouds without
10 ACA, for which we use the MODIS operational LUT, and clouds with ACA, for which we
use the one developed by Meyer et al. (2013). In the operational MODIS retrieval, the
reflectance LUT of cloud without ACA is used to interpret the reflectance of all clouds,
including those affected by ACA. Based on this fact, we first infer the “observed” cloud
reflectance (after atmospheric correction) by interpolating the reflectance LUT of cloud
15 without ACA corresponding to the biased COD. Then, we use the “observed” cloud
reflectance and ACA-affected LUT (derived based on CALIOP AOD) to determine the
corrected COD. This COD correction process is performed for every combination of
COD bin in $p(\tau_c)$ and AOD bin in $p(\tau_a)$. In the final step we resample the corrected
CODs to obtain the corrected $p(\tau_c)$.

20 It should be noted that because different aerosol types may have different impacts
on MODIS COD retrievals, the above COD correction process is aerosol-type depen-
dent. In this study, we use light-absorbing aerosols as an example to illustrate our
method, and for validation purposes we use the aerosol model developed in Meyer
et al. (2013) for the development of LUTs for DRE computation and COD correction.

25 However, the LUTs can be easily extended to other aerosol models. In fact, as part of
ongoing research, we are extending our LUTs to include all six operational CALIOP
aerosol models as described in (Omar et al., 2009).

10003

4 Implementation and validation of new DRE estimation scheme

Each year during austral winter, dry season biomass burning activities throughout southern Africa inject large amounts of smoke into the troposphere (Eck et al., 2003; Ichoku et al., 2003; Myhre et al., 2003). Prevailing easterly winds during this season often transport the smoke westward off the continent, over the ocean, where extensive marine boundary layer clouds persist for most of the year. Under the descending branch of the Hadley cell, the air mass above the boundary layer is quite dry. Due to the lack of efficient wet scavenging, the transported aerosol layers can remain suspended in the atmosphere for days, creating a near-persistent smoke layer above the stratocumulus deck over the southeastern Atlantic Ocean during this time (Chand et al., 2009; Devasthale and Thomas, 2011; Keil and Haywood, 2003; Wilcox, 2010).

To validate our method, we have compared the DRE of above-cloud light-absorbing aerosols in this region with pixel-level computations from Meyer et al. (2013). Figure 3a shows the seasonal mean (August/September 2007–2011) instantaneous TOA DRE of above-cloud smoke and polluted dust based on the pixel-level computations from Meyer et al. (2013). Figure 3b shows the corresponding instantaneous TOA aerosol radiative forcing efficiency (RFE) defined as the DRE per unit AOD. The DRE and RFE results computed using our method described in the previous section are shown in Fig. 3c and d, respectively. Evidently, both DRE and RFE computed using our new method agree closely with the pixel-level computations. Figure 4 shows the meridional mean DRE and RFE for the region based on the results in Fig. 3. Not surprisingly, the results based on the two methods are almost identical. Note that the CODs used in the computations for Figs. 3 and 4 are directly from the MODIS products without COD correction. We have also compared the DRE and RFE from the two methods based on the corrected COD and achieved again very good agreement (these results are not shown here because they are quite similar to those in Figs. 3 and 4). The seasonal and regional mean DRE and RFE, based on the corrected COD, from the pixel-level computation method in Meyer et al. (2013) are 6.63 W m^{-2} and $55.97 \text{ W m}^{-2} \text{ AOD}^{-1}$, respectively.

10004

(see Table 2). The corresponding values from our new method are 6.39 W m^{-2} and $53.77 \text{ W m}^{-2} \text{ AOD}^{-1}$, respectively. As shown clearly in Figs. 3 and 4 and Table 2, the DRE inferred from our new method agrees very well with the pixel-level computations. Furthermore, the difference between the two methods is much smaller than, for example, the uncertainty associated with CALIOP retrieval biases. Recent studies found about a factor of two difference between CALIOP nighttime and daytime AOD retrievals (Chand et al., 2008; Meyer et al., 2013). If this difference is considered as CALIOP AOD retrieval uncertainty, it could lead to 30 %~50 % uncertainty in ACA DRE computation (see Fig. 12 of Meyer et al., 2013).

10 5 Summary and discussion

Recent advances in satellite-based remote sensing, in particular the launch of the space-borne lidar CALIOP, have provided an unprecedented opportunity for studying the radiative effects of above-cloud aerosol (ACA). However, the methodologies used in recent studies for computing the ACA DRE appear to be either oversimplified (e.g., Chand et al., 2009; Oikawa et al., 2013) or too cumbersome (e.g., Meyer et al., 2013). This paper describes a novel method recently developed for computing the shortwave DRE of above-cloud aerosols over ocean. Our method has several unique features compared to methods used in previous studies: (1) it takes sub-grid scale cloud and aerosol variation into account in DRE computations, similar to Meyer et al. (2013); (2) it also treats the overlapping of aerosol and cloud rigorously by utilizing the joint histogram of COD and CTP in the MODIS level-3 cloud product; (3) it differs from Meyer et al. (2013) in its reliance on grid-level cloud statistics (i.e., COD-CTP joint histogram), instead of pixel-level products, and utilizes pre-computed look-up tables for ACA DRE computations, making it thus much more efficient than pixel-level computations. As shown in Figs. 3 and 4 and Table 2, DRE computed using our method agrees well with the pixel-level computations in Meyer et al. (2013).

10005

In addition to the Southeast Atlantic region, we have recently begun investigating the DRE of above-cloud light-absorbing aerosols for global ocean. Some preliminary results are shown in Fig. 5. We first derived the daily grid-level statistics of above-cloud AOD and below cloud COD, as well as the corresponding ACA DRE, using the method described above and then aggregated the daily means to annual mean. The temporal aggregation is weighted by the number of ACA pixels in each day during 2007–2010. For example, the annual mean ACA DRE in Fig. 5c is aggregated from daily mean based on the following equation:

$$\overline{\langle \text{DRE} \rangle_{\text{ACA}}} = \frac{\sum_i N_i \cdot \langle \text{DRE}_i \rangle_{\text{ACA}}}{\sum_i N_i}, \quad (3)$$

where $\langle \text{DRE}_i \rangle_{\text{ACA}}$ is mean instantaneous ACA DRE in each day averaged over ACA pixels, N_i is the number of ACA pixels in the grid box in each day, and $\overline{\langle \text{DRE} \rangle_{\text{ACA}}}$ is the annual mean instantaneous ACA DRE shown in Fig. 5c. In Fig. 5a a global map is shown of the annual mean 550 nm AOD of above cloud smoke and polluted dust derived based on 4 yr (2007–2010) of CALIOP aerosol and cloud layer products. Similar to Devasthale and Thomas (2011), we note several “hotspots” of ACA over the Southeast Atlantic, the East-Central Atlantic off the western coast of Saharan Africa, the Arabian sea, and the North Pacific basin off the coast of eastern Asia. It is interesting to note that the ACA AOD over the east-central Atlantic and Arabian Sea is noticeably larger than that over the southeast Atlantic and North Pacific basin. Figure 5b shows the annual mean below-aerosol COD derived from the MODIS daily level-3 cloud product using the method described in Sect. 3. A notable feature in the figure is that the below-aerosol COD over the North Pacific basin is significantly larger than that over other ACA regions. Figure 5c shows the annual mean shortwave DRE at TOA aggregated from daily values due to ACA smoke and polluted dust over the global ocean. It is intriguing to see that the DRE of ACA over the North Pacific basin is significantly larger than that over the southeast Atlantic, which is in turn larger than the DRE over

10006

the east-central Atlantic and the Arabian Sea. In fact, some negative DREs are observed in the latter two regions. This is interesting because the above-cloud AOD over these regions is actually larger, while the below-aerosol COD over these regions is smaller, in comparison with the counterparts over the southeast Atlantic and North Pacific basin. Therefore, the preliminary results seem to suggest that the variability of DRE of ACA is modulated by COD, rather than AOD, although it should be noted that we have focused only on the light-absorbing aerosols, i.e., smoke and polluted dust, and assumed the same broadband scattering properties for them as in Meyer et al. (2013). Future research is needed to study the impact of aerosol type and scattering properties on the temporal-spatial variation of DRE on a global scale. Nevertheless, the preliminary results shown in Fig. 5 clearly demonstrate the usefulness of our new method for global study.

It should be noted that this study, and previous ones using CALIOP observations (e.g., Chand et al., 2008; Meyer et al., 2013; Oikawa et al., 2013), are limited by the capabilities of CALIOP. Arguably, some aerosols exist above every cloud. However, not all ACA can be detected by CALIOP due to its inherent limitations. Some ACAs are simply too optically thin to be detected, though their radiative effects are also expected to be small. There are also other possibilities. For example, a confined aerosol layer has larger volume backscatter than a vertically stretched layer, even if the aerosol amounts are the same, and therefore is more easily detected by CALIOP. Passive sensors, on the other hand, are less affected by the vertical distribution of ACA because they observe column-integrated scattering by aerosols. Recently, several novel techniques have been developed to detect and retrieve ACA properties using passive sensors. Waquet et al. (2009) developed a method based on multi-angular polarization measurements from POLDER (Polarization and Directionality of the Earth Reflectances) to retrieve the AOD of above-cloud smoke. This method has recently been extended to include both smoke and dust aerosols (Waquet et al., 2013). Most recently, Jethva et al. (2013) demonstrated a color ratio method to retrieve the above-cloud AOD based on MODIS multiple spectral cloud reflectance measurements. A review of the emerging

10007

satellite-based observations of above-cloud aerosols can be found in Yu and Zhang (2013). The capabilities and limitations of the passive techniques need to be systematically studied through inter-comparison and comparison with CALIOP observations, but they may provide a complementary perspective on ACA. Note that passive imagers have much larger spatial coverage than CALIOP, which makes calculations of the DRE at the pixel level computationally expensive. In this regard, our method satisfies the need for efficiency of ACA DRE computations based on passive imager retrievals.

As a final remark, we would like to point out that the ACA DRE discussed in this study is still a few steps away from the all-sky aerosol radiative effect ($\langle \text{DRE} \rangle_{\text{all-sky}}$). For a given grid box, the $\langle \text{DRE} \rangle_{\text{all-sky}}$ can be decomposed into the sum of clear-sky and cloudy-sky DRE:

$$\langle \text{DRE} \rangle_{\text{all-sky}} = (1 - f_c) \cdot \langle \text{DRE} \rangle_{\text{clear}} + f_c \cdot f_{\text{ACA}} \cdot \langle \text{DRE} \rangle_{\text{ACA}}, \quad (4)$$

where f_c is the cloud fraction, $\langle \text{DRE} \rangle_{\text{clear}}$ is the DRE averaged over the clear-sky portion of the grid box, f_{ACA} is the fraction of cloudy pixels with ACA detected by CALIOP or other sensors, and $\langle \text{DRE} \rangle_{\text{ACA}}$ is the DRE averaged over all ACA containing pixels. It is important to note an implicit assumption made in Eq. (4), that is, when a distinct ACA layer is not detected, the DRE is zero. Different sensors (or different retrieval algorithms for the same sensor) may have different sensitivities to ACA and therefore provide different estimates of f_{ACA} and $\langle \text{DRE} \rangle_{\text{ACA}}$. For example, one sensor may only retrieve ACA for optically thick clouds. This sensor would retrieve a larger $\langle \text{DRE} \rangle_{\text{ACA}}$, but a smaller f_{ACA} , in comparison with another sensor that is able to retrieve ACA for all clouds. Therefore, when comparing the ACA or all-sky DRE estimated based on different instruments or algorithms, it is important to compare both f_{ACA} and $\langle \text{DRE} \rangle_{\text{ACA}}$ terms in Eq. (4).

Acknowledgements. This research is supported by NASA via grant NNX14AB21G. The authors are grateful to NASA for providing MODIS and CALIOP products used in this study.

10008

References

Abel, S. J., Highwood, E. J., Haywood, J. M., and Stringer, M. A.: The direct radiative effect of biomass burning aerosols over southern Africa, *Atmos. Chem. Phys.*, 5, 1999–2018, doi:10.5194/acp-5-1999-2005, 2005.

5 Ackerman, S., Strabala, K., Menzel, W., Frey, R., Moeller, C., and Gumley, L.: Discriminating clear sky from clouds with MODIS, *J. Geophys. Res.*, 103, 32141–32157, 1998.

Chand, D., Anderson, T. L., Wood, R., Charlson, R. J., Hu, Y., Liu, Z., and Vaughan, M.: Quantifying above-cloud aerosol using spaceborne lidar for improved understanding of cloudy-sky direct climate forcing, *J. Geophys. Res.*, 113, D13206, doi:10.1029/2007JD009433, 2008.

10 Chand, D., Wood, R., Anderson, T. L., Satheesh, S. K., and Charlson, R. J.: Satellite-derived direct radiative effect of aerosols dependent on cloud cover, *Nat. Geosci.*, 2, 181–184, doi:10.1038/ngeo437, 2009.

Clough, S. A., Shephard, M. W., Mlawer, E. J., Delamere, J. S., Iacono, M. J., Cady-Pereira, K., Boukabara, S., and Brown, P. D.: Atmospheric radiative transfer modeling: a summary of the AER codes, *J. Quant. Spectrosc. Ra.*, 91, 233–244, 2005.

Coddington, O. M., Pilewskie, P., Redemann, J., Platnick, S., Russell, P. B., Schmidt, K. S., Gore, W. J., Livingston, J., Wind, G., and Vukicevic, T.: Examining the impact of overlying aerosols on the retrieval of cloud optical properties from passive remote sensing, *J. Geophys. Res.*, 115, D10211, doi:10.1029/2009JD012829, 2010.

20 Costantino, L. and Bréon, F.-M.: Aerosol indirect effect on warm clouds over South-East Atlantic, from co-located MODIS and CALIPSO observations, *Atmos. Chem. Phys.*, 13, 69–88, doi:10.5194/acp-13-69-2013, 2013a.

Costantino, L. and Bréon, F.-M.: Satellite-based estimate of aerosol direct radiative effect over the South-East Atlantic, *Atmos. Chem. Phys. Discuss.*, 13, 23295–23324, doi:10.5194/acpd-13-23295-2013, 2013b.

Devasthale, A. and Thomas, M. A.: A global survey of aerosol-liquid water cloud overlap based on four years of CALIPSO-CALIOP data, *Atmos. Chem. Phys.*, 11, 1143–1154, doi:10.5194/acp-11-1143-2011, 2011.

Eck, T. F., Holben, B. N., Ward, D. E., Mukelabai, M. M., Dubovik, O., Smirnov, A., Schafer, J. S., Hsu, N. C., Piketh, S. J., Queface, A., Roux, J. L., Swap, R. J., and Slutsker, I.: Variability of biomass burning aerosol optical characteristics in southern Africa during the SAFARI 2000

10009

dry season campaign and a comparison of single scattering albedo estimates from radiometric measurements, *J. Geophys. Res.*, 108, 8477, doi:10.1029/2002JD002321, 2003.

Hartmann, D., Holton, J., and Fu, Q.: The heat balance of the tropical tropopause, cirrus, and stratospheric dehydration, *Geophys. Res. Lett.*, 28, 1969–1972, 2001.

5 Haywood, J. M., Osborne, S. R., and Abel, S. J.: The effect of overlying absorbing aerosol layers on remote sensing retrievals of cloud effective radius and cloud optical depth, *Q. J. Roy. Meteor. Soc.*, 130, 779–800, doi:10.1256/qj.03.100, 2004.

Hu, Y., Vaughan, M., Liu, Z., Lin, B., Yang, P., Flittner, D., Hunt, B., Kuehn, R., Huang, J., Wu, D., Rodier, S., Powell, K., Trepte, C., and Winker, D.: The depolarization – attenuated backscatter relation: CALIPSO lidar measurements vs. theory, *Opt. Express*, 15, 5327, doi:10.1364/OE.15.005327, 2007.

Hubanks, P. A., King, M. D., Platnick, S., and Pincus, R.: MODIS atmosphere L3 gridded product algorithm theoretical basis document, *Algorithm Theor. Basis Doc. ATBD-MOD*, 30, 2008.

Iacono, M. J., Delamere, J. S., Mlawer, E. J., Shephard, M. W., Clough, S. A., and Collins, W. D.: Radiative forcing by long-lived greenhouse gases: calculations with the AER radiative transfer models, *J. Geophys. Res.*, 113, D13103, doi:10.1029/2008JD009944, 2008.

Ichoku, C., Remer, L. A., Kaufman, Y. J., Levy, R., Chu, D. A., Tanré, D., and Holben, B. N.: MODIS observation of aerosols and estimation of aerosol radiative forcing over southern Africa during SAFARI 2000, *J. Geophys. Res.*, 108, 8499, doi:10.1029/2002JD002366, 2003.

Jethva, H., Torres, O., Remer, L. A., and Bhartia, P. K.: A color ratio method for simultaneous retrieval of aerosol and cloud optical thickness of above-cloud absorbing aerosols from passive sensors: application to MODIS measurements, *IEEE T. Geosci. Remote*, 51, 3862–3870, 2013.

25 Keil, A. and Haywood, J. M.: Solar radiative forcing by biomass burning aerosol particles during SAFARI 2000: a case study based on measured aerosol and cloud properties, *J. Geophys. Res.*, 108, 8467, doi:10.1029/2002JD002315, 2003.

King, M. D., Menzel, W. P., Kaufman, Y. J., Tanre, D., Gao, B.-C., Platnick, S., Ackerman, S. A., Remer, L. A., Pincus, R., and Hubanks, P. A.: Cloud and aerosol properties, precipitable water, and profiles of temperature and water vapor from MODIS, *IEEE T. Geosci. Remote*, 41, 442–458, doi:10.1109/TGRS.2002.808226, 2003.

10010

King, M. D., Platnick, S., Menzel, W. P., Ackerman, S. A., and Hubanks, P. A.: Spatial and temporal distribution of clouds observed by MODIS onboard the terra and aqua satellites, *IEEE T. Geosci. Remote*, 51, 3826–3852, doi:10.1109/TGRS.2012.2227333, 2013.

Kistler, R., Collins, W., Saha, S., White, G., Woollen, J., Kalnay, E., Chelliah, M., Ebisuzaki, W., Kanamitsu, M., Kousky, V., van den Dool, H., Jenne, R., and Fiorino, M.: The NCEP-NCAR 50-year reanalysis: monthly means CD-ROM and documentation, *B. Am. Meteorol. Soc.*, 82, 247–267, doi:10.1175/1520-0477(2001)082<0247:TNNYRM>2.3.CO;2, 2001.

Levy, R. C., Remer, L. A., Tanre, D., Mattoe, S., and Kaufman, Y. J.: Algorithm for remote sensing of tropospheric aerosol over dark targets from MODIS: collections 005 and 051: revision 2, MODIS Algorithm Theoretical Basis Document for the MOD04_L2 Product, 2009.

Liu, Z., Vaughan, M., Winker, D., Kittaka, C., Getzewich, B., Kuehn, R., Omar, A., Powell, K., Trepte, C., and Hostetler, C.: The CALIPSO Lidar cloud and aerosol discrimination: version 2 algorithm and initial assessment of performance, *J. Atmos. Ocean. Tech.*, 26, 1198–1213, doi:10.1175/2009JTECHA1229.1, 2009.

Menzel, P., Frey, R., Baum, B., and Zhang, H.: Cloud top properties and cloud phase algorithm theoretical basis document, available at: http://modis.gsfc.nasa.gov/data/atbd/atbd_mod04.pdf (last access: 14 November 2013), 2006.

Menzel, W., Smith, W., and Stewart, T.: Improved cloud motion wind vector and altitude assignment using VAS, *J. Appl. Meteorol.*, 22, 377–384, 1983.

Meyer, K., Platnick, S., Oreopoulos, L., and Lee, D.: Estimating the direct radiative effect of absorbing aerosols overlying marine boundary layer clouds in the southeast Atlantic using MODIS and CALIOP, *J. Geophys. Res.-Atmos.*, 118, 4801–4815, doi:10.1002/jgrd.50449, 2013.

Myhre, G., Berntsen, T. K., Haywood, J. M., Sundet, J. K., Holben, B. N., Johnsrud, M., and Stordal, F.: Modeling the solar radiative impact of aerosols from biomass burning during the Southern African Regional Science Initiative (SAFARI-2000) experiment, *J. Geophys. Res.*, 108, 8501, doi:10.1029/2002JD002313, 2003.

Nakajima, T. and King, M.: Determination of the optical thickness and effective particle radius of clouds – Part 1: Theory, *J. Atmos. Sci.*, 47, 1878–1893, 1990.

Oikawa, E., Nakajima, T., Inoue, T., and Winker, D.: A study of the shortwave direct aerosol forcing using ESSP/CALIPSO observation and GCM simulation, *J. Geophys. Res.*, 118, 3687–3708, doi:10.1002/jgrd.50227, 2013.

10011

Omar, A. H., Winker, D. M., Vaughan, M. A., Hu, Y., Trepte, C. R., Ferrare, R. A., Lee, K.-P., Hostetler, C. A., Kittaka, C., and Rogers, R. R.: The CALIPSO automated aerosol classification and lidar ratio selection algorithm, *J. Atmos. Ocean. Tech.*, 26, 1994–2014, 2009.

Oreopoulos, L., Cahalan, R. F., and Platnick, S.: The plane-parallel albedo bias of liquid clouds from MODIS observations, *J. Climate*, 20, 5114–5125, doi:10.1175/JCLI4305.1, 2007.

Platnick, S., King, M., Ackerman, S., Menzel, W., Baum, B., Riedi, J., and Frey, R.: The MODIS cloud products: algorithms and examples from Terra, *IEEE T. Geosci. Remote*, 41, 459–473, 2003.

Schulz, M., Textor, C., Kinne, S., Balkanski, Y., Bauer, S., Berntsen, T., Berglen, T., Boucher, O., Dentener, F., Guibert, S., Isaksen, I. S. A., Iversen, T., Koch, D., Kirkevåg, A., Liu, X., Montanaro, V., Myhre, G., Penner, J. E., Pitari, G., Reddy, S., Selander, Ø., Stier, P., and Takemura, T.: Radiative forcing by aerosols as derived from the AeroCom present-day and pre-industrial simulations, *Atmos. Chem. Phys.*, 6, 5225–5246, doi:10.5194/acp-6-5225-2006, 2006.

Stier, P., Schutgens, N. A. J., Bellouin, N., Bian, H., Boucher, O., Chin, M., Ghan, S., Huneeus, N., Kinne, S., Lin, G., Ma, X., Myhre, G., Penner, J. E., Randles, C. A., Samset, B., Schulz, M., Takemura, T., Yu, F., Yu, H., and Zhou, C.: Host model uncertainties in aerosol radiative forcing estimates: results from the AeroCom Prescribed intercomparison study, *Atmos. Chem. Phys.*, 13, 3245–3270, doi:10.5194/acp-13-3245-2013, 2013.

Twomey, S.: Atmospheric aerosols, Elsevier Scientific Publishing Co., New York, NY, 1977.

Vaughan, M. A., Powell, K. A., Winker, D. M., Hostetler, C. A., Kuehn, R. E., Hunt, W. H., Getzewich, B. J., Young, S. A., Liu, Z., and McGill, M. J.: Fully automated detection of cloud and aerosol layers in the CALIPSO lidar measurements, *J. Atmos. Ocean. Tech.*, 26, 2034–2050, doi:10.1175/2009JTECHA1228.1, 2009.

Waquet, F., Riedi, J., Labonne, L. C., Goloub, P., Cairns, B., Deuzé, J. L., and Tanré, D.: Aerosol remote sensing over clouds using a-train observations, *J. Atmos. Sci.*, 66, 2468–2480, doi:10.1175/2009JAS3026.1, 2009.

Waquet, F., Cornet, C., Deuzé, J.-L., Dubovik, O., Ducos, F., Goloub, P., Herman, M., Lapyonok, T., Labonne, L. C., Riedi, J., Tanré, D., Thieuleux, F., and Vanbaucx, C.: Retrieval of aerosol microphysical and optical properties above liquid clouds from POLDER/PARASOL polarization measurements, *Atmos. Meas. Tech.*, 6, 991–1016, doi:10.5194/amt-6-991-2013, 2013.

Wilcox, E. M.: Stratocumulus cloud thickening beneath layers of absorbing smoke aerosol, *Atmos. Chem. Phys.*, 10, 11769–11777, doi:10.5194/acp-10-11769-2010, 2010.

10012

Winker, D. M., Vaughan, M. A., Omar, A., Hu, Y., Powell, K. A., Liu, Z., Hunt, W. H., and Young, S. A.: Overview of the CALIPSO mission and CALIOP data processing algorithms, *J. Atmos. Ocean. Tech.*, 26, 2310–2323, 2009.

Winker, D. M., Tackett, J. L., Getzewich, B. J., Liu, Z., Vaughan, M. A., and Rogers, R. R.: The global 3-D distribution of tropospheric aerosols as characterized by CALIOP, *Atmos. Chem. Phys.*, 13, 3345–3361, doi:10.5194/acp-13-3345-2013, 2013.

Wiscombe, W. J.: Improved Mie scattering algorithms, *Appl. Optics*, 19, 1505–1509, doi:10.1364/AO.19.001505, 1980.

Young, S. A. and Vaughan, M. A.: The retrieval of profiles of particulate extinction from Cloud-Aerosol Lidar Infrared Pathfinder Satellite Observations (CALIPSO) data: algorithm description, *J. Atmos. Ocean. Tech.*, 26, 1105–1119, doi:10.1175/2008JTECHA1221.1, 2008.

Yu, H. and Zhang, Z.: New directions: emerging satellite observations of above-cloud aerosols and direct radiative forcing, *Atmos. Environ.*, 72, 36–40, doi:10.1016/j.atmosenv.2013.02.017, 2013.

Yu, H., Kaufman, Y. J., Chin, M., Feingold, G., Remer, L. A., Anderson, T. L., Balkanski, Y., Belouin, N., Boucher, O., Christopher, S., DeCola, P., Kahn, R., Koch, D., Loeb, N., Reddy, M. S., Schulz, M., Takemura, T., and Zhou, M.: A review of measurement-based assessments of the aerosol direct radiative effect and forcing, *Atmos. Chem. Phys.*, 6, 613–666, doi:10.5194/acp-6-613-2006, 2006.

Zelinka, M. D., Klein, S. A., and Hartmann, D. L.: Computing and partitioning cloud feedbacks using cloud property histograms. Part I: Cloud radiative kernels, *J. Climate*, 25, 3715–3735, doi:10.1175/JCLI-D-11-00248.1, 2012.

10013

Table 1. Quality control metrics used for screening the CALIOP aerosol layer product.

	Criterion
CAD_score	< -30
Horizontal_averaging	< 20 km
Extinction_QC_532	0 or 1
Feature_Optical_Depth_Uncertainty_532	< -99.5

10014

Table 2. Regional and seasonal mean values of instantaneous DRE and RFE based on the pixel-level computation and the new method.

	DRE [W m^{-2}] Bias adjusted (unadjusted)	RFE [$\text{W m}^{-2} \text{AOD}^{-1}$] Bias adjusted (unadjusted)
Pixel computation	6.63 (5.92)	55.97 (50.34)
New Method	6.39 (5.77)	53.77 (50.22)

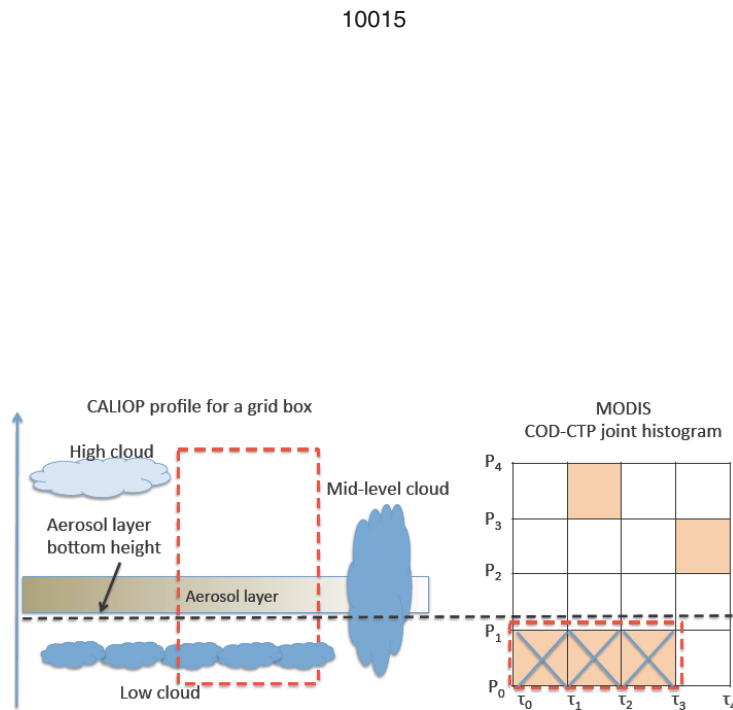


Fig. 1. A schematic example to illustrate how CALIOP aerosol layer height information is used in our method to determine the population of liquid-phase clouds below the aerosol layer in the MODIS COD-CTP joint histogram.

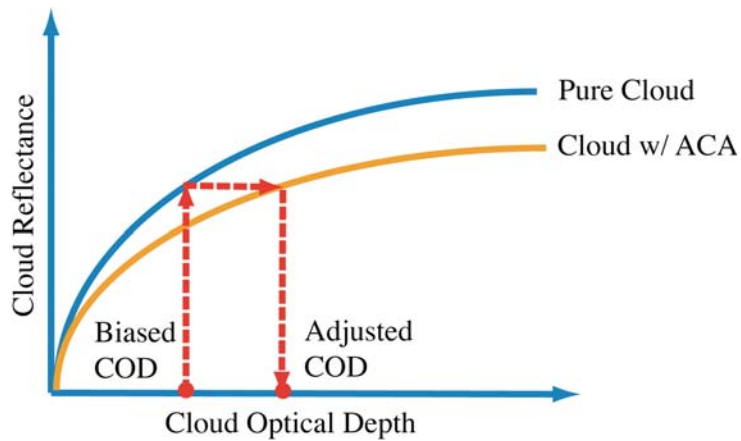


Fig. 2. A schematic illustration of our fast scheme to correct the COD retrieval bias in the MODIS cloud product due to overlying aerosol contamination.

10017

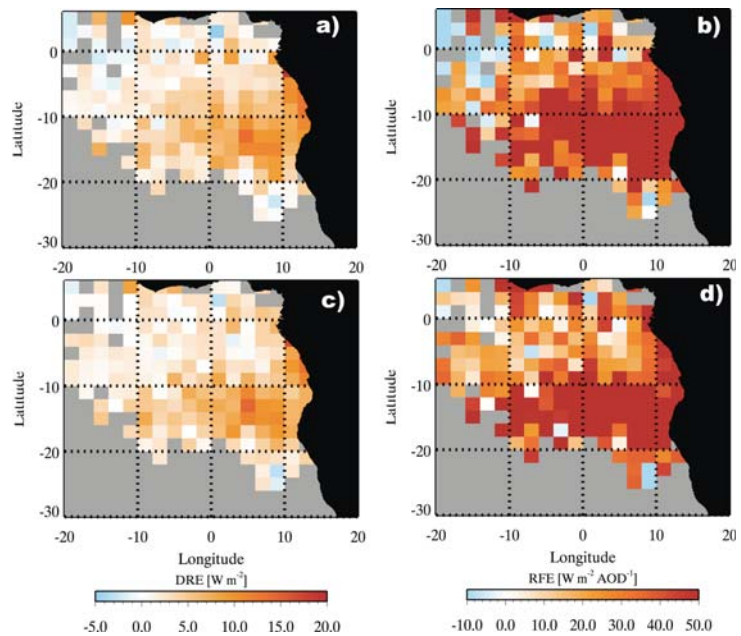


Fig. 3. (a) Seasonal mean (August/September 2007–2011) instantaneous TOA DRE of above-cloud smoke and polluted dust based on the pixel-level computations from Meyer et al. (2013); (b) seasonal mean instantaneous TOA aerosol RFE (i.e., DRE per AOD) from Meyer et al. (2013); (c) same as (a), but based on the new method; (d) same as (b), but based on the new method.

10018

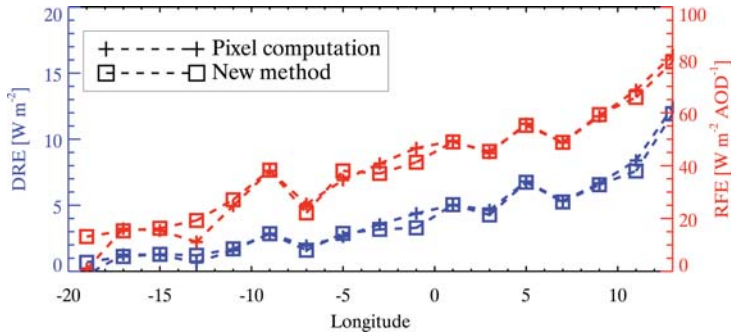


Fig. 4. Meridional mean DRE and RFE for the region based on the results in Fig. 3. Lines with cross symbol correspond to pixel computations from Meyer et al. (2013). Lines with square symbol correspond to results based on the new method.

10019

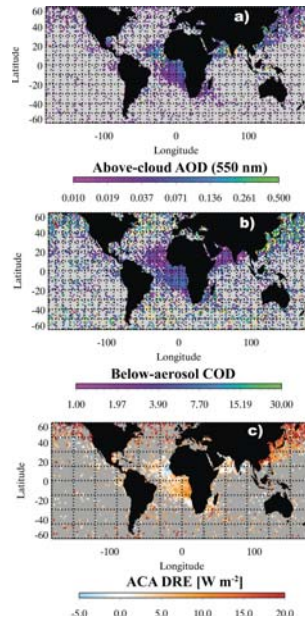


Fig. 5. (a) Annual mean AOD (at 550 nm) of above-cloud light-absorbing aerosols (i.e., smoke and polluted dust) derived from 4 yr (2007~2010) of the CALIOP 5 km aerosol and cloud layer products. (b) Annual mean below-aerosol COD derived from the MODIS daily level-3 COD-CTP joint histogram. (c) Annual mean instantaneous TOA DRE of above-cloud light-absorbing aerosols derived using the new method.

10020